Polymer decoration of carbon support to boost Pt-catalyzed hydrogen generation activity and durability

Wenyao Chen,[a] Wenzhao Fu,[a] Bingxu Chen,[a] Chong Peng,[b,*] Gang Qian,[a] De Chen,[c] Xuezhi Duan,[a,*] Xinggui Zhou[a]

[a]*State Key Laboratory of Chemical Engineering, East China University of Science and Technology, 130 Meilong Road, Shanghai 200237, China*

[b]*Dalian Research Institute of Petroleum and Petrochemicals, SINOPEC, Liaoning, Dalian 116045, China*

[c]*Department of Chemical Engineering, Norwegian University of Science and Technology, N-7491 Trondheim, Norway*

[*]To whom correspondence should be addressed. Tel.: +86-21-64250937; E-mail: xzduan@ecust.edu.cn; pengchong.fshy@sinopec.com.

ABSTRACT: Decorating the catalyst support with organic moieties to integrate multiple functionalities into metal particles offers a unique platform to promote the catalytic performance. Here, we report a mechanism-driven strategy to functionalize CNT with dual polymers, endowing the supported Pt catalyst with simultaneously enhanced hydrogen generation activity and durability. Kinetics analysis, multiple characterization and DFT calculations reveal that the PDDA acts as electron-acceptor to capture electrons from the Pt particles toward strengthened adsorption of reactants, while the PVP acts as structure-directing agent to induce the catalyst morphology evolution with a preferential exposure of Pt(111) active sites. Such electronic and geometric synergy by co-functionalizing PDDA and PVP gives rise to a 3-fold increase in the hydrogen generation activity, together with remarkably improved catalytic durability due to the suppressed adsorption of $B(OH)_4^-$ over the Pt(111). The strategy reported here might shed new lights on establishing the functionalization protocols to design carbon supported metal catalysts with the targeted properties.

Keywords: Carbon supported metal catalysts; Polymer functionalization; Electronic and geometric synergy; Hydrogen generation rate; Catalyst durability

1. Introduction

Carbon nanomaterials are distinguished as catalyst support by their fascinating properties, e.g., high electron conductivity and tunable surface chemistry, which trigger enormous interests in heterogeneous catalysis [1-3]. Generally, subtle functionalization on the carbon surface is necessary and critical to alter its chemically inert nature and enhance the interaction with the supported metal for practical catalytic process [4-6]. Compared with covalent functionalization via strong acidic oxidation, noncovalent functionalization can preserve the structural and electronic integrity of carbon, while endows it with the versatile functionality [7-9]. Recent studies have found that the noncovalent functionalization also gives rise to unique surface, interfacial and electronic properties of carbon supported metal catalysts and thereby promotes the catalytic performance [10-15]. Hence, an attempt is highly desirable to clarify the mastery of their electronic and geometric nature for guiding the rational design and manipulation of noncovalently functionalized carbon supported catalysts.

The probe reaction chosen in the present study is catalytic hydrolytic dehydrogenation of ammonia borane (NH_3BH_3, AB) over Pt catalyst supported on the noncovalently-functionalized carbon support developed below. This process, known as a structure-sensitive reaction, has been widely employed as a model reaction to understand the catalyst structure-performance relations [16-20], and as a promising route to produce hydrogen at mild conditions for fuel cell applications [21-24]. Such structure sensitivity originates from the chemistry mainly happened on the Pt(111) active sites [25], and the ability to adsorb and activate reactants [26] as well as promote

the rate determining step of $NH_3BH_2*+H_2O*\rightarrow NH_3BH_2OH*+H*$ [27,28]. Moreover, in consideration of the serious catalyst deactivation including metal agglomeration and B-containing by-products adsorption [25], it is worthwhile and timely to design the noncovalently functionalized carbon supported Pt catalyst with the targeted properties for simultaneously enhancing the hydrogen generation rate and catalyst durability.

The objective of this study is to develop a mechanism-driven strategy by using dual polymers to noncovalently functionalize carbon nanotubes (CNT) for making full use of the supported Pt electronic and geometric synergy. Based on the unique characteristics of polymers [10,12], the water-soluble polycation, poly(diallyldimethylammonium chloride) (PDDA), and polyanion, poly(vinylsulfonic acid, sodium salt) (PVS), were chosen to manipulate the Pt electronic properties, while polyvinyl pyrrolidone (PVP) chosen to tailor the Pt geometric properties. A combined kinetics analysis, multiple characterization and DFT calculations was conducted to clarify the underlying nature of the polymer functionalization. As a result, the dual PDDA-PVP functionalized CNT appears to be a promising support for obtaining the Pt particles with fantastic catalytic properties toward simultaneously enhanced hydrogen generation activity and durability. Our work provides for the first time the link of preparation (support decoration), structure (metal electron and geometry induction) and property (catalytic behaviors and kinetics) for carbon supported Pt catalysts used for mild hydrogen generation from ammonia borane.

2. Experimental

2.1. *Functionalization of CNT*

The multi-walled carbon nanotubes (CNT) with the purity of >98% were purchased from Beijing Cnano Technology Limited as the catalyst support. The presence of oxygen containing groups over the CNT could endow it with the hydrophilic nature for the functionalization of water-soluble polymers. Herein, three kinds of water-soluble polymers, i.e., poly(diallyldimethylammonium chloride) (PDDA, Sigma-Aldrich Co. Ltd.), poly(vinylsulfonic acid, sodium salt) (PVS, Sigma-Aldrich Co. Ltd.) and polyvinyl pyrrolidone (PVP, Sinopharm Chemical Reagent Co. Ltd), were used for non-covalent functionalization of CNT. Both the hexachloroplatinic acid ($H_2PtCl_6 \cdot 6H_2O$) and sodium chloride (NaCl) were purchased from the Sinopharm Chemical Reagent Co. Ltd.

The procedures for non-covalent functionalization of CNT are as following: a given amount of polymers, i.e., PDDA, PVS and PVP, as well as sodium chloride were first dissolved in 500 mL deionized water to obtain the solution with the concentration of polymer (0.5 wt%) and NaCl (1.0 wt%). Then, 0.15 g CNT was mixed with the above solution under ultrasonication for 1 h, followed by magnetically stirring for 12 h at room temperature. After that, the suspended solution was filtered and washed by deionized water several times to remove the excess polymer and sodium chloride. The samples were dried in a vacuum oven at 70 ºC for 24 h, and the as-obtained functionalized CNT was denoted as CNT-x, which x represents the type of the polymers.

2.2. Catalyst preparation and testing

The pristine and functionalized CNT supported Pt catalysts were prepared by

incipient wetness impregnation. In detail, an aqueous solution of H_2PtCl_6 was mixed with a certain amount of CNT with Pt loading of 1.5 wt%. The as-obtained catalyst precursors were dried at room temperature for 12 h, and then at 70 °C under vacuum for another 12 h. The resultant catalyst precursors were in-situ reduced with the ammonia borane reactant under mild conditions rather than the H_2 thermal reduction. Hence, the flexible nature of the polymers was still kept, and the carbonization of the polymers was inhibited for avoiding the metal nanoparticles encapsulation during the thermal reduction treatment [29].

For the typical catalytic testing, 0.1 g catalyst precursor was preloaded in a 50 mL three-necked flask with a Teflon-coated stir bar. Then, the flask was transferred in a water bath at 30 °C with a magnetic stirrer, and connected to a water-filled gas burette to measure the volume of evolved hydrogen based on the discharged water. The reaction was initialized by injecting an aqueous ammonia borane solution (5 mL and 0.01 g·mL^{-1}) into the flask via a syringe under vigorous stirring to exclude the mass-transfer limitations. After a short induction period, the Pt nanoparticles were in-situ generated to catalyze hydrolytic dehydrogenation of ammonia borane. A mass balance was used to weigh the amount of discharged water, which could be further converted into the volume of evolved hydrogen. After the completion of hydrogen generation, the ammonia borane reduced catalyst was filtered from the spent solution and washed with deionized water several times, followed by dried under vacuum at 30 °C for characterization.

Kinetics experiments were conducted at various temperatures (25, 30, 35 and 40 °C)

to obtain the activation energy. To investigate the durability of different catalysts, another new ammonia borane solution (5 mL and 0.01 g mL^{-1}) was quickly injected into the flask after the completion of the last cycle, and such operation was repeated for five times. After the durability testing, the deactivated catalyst was filtered from the spent solution and washed with deionized water several times, followed by dried under vacuum at 30 °C for characterization.

2.3. Catalytic characterization

Fourier transform infrared (FTIR) spectra were measured with a spectrometer (Model Spectrum 100). Thermal gravimetric analysis (TGA) were performed using a TA Instrument (SDT Q600 thermogravimetric analyser), where thermograms were collected from room temperature to 800 °C with a heating rate of 10 °C·min^{-1} under N_2. Raman spectra were obtained with a LabRAM-HR instrument (Horiba Jobin Yvon) coupled with an argon ion Ar laser (514 nm) for excitation. X-ray diffraction (XRD) measurements were conducted on an X-ray diffractometer (Rigaku D/Max 2550VB/PC diffractometer) at room temperature with a Cu K$_\alpha$ radiation source. High angle annular dark field scanning transmission electron microscopy (HAADF-STEM) imaging and energy dispersive X-ray spectroscopy (EDS) elemental mapping were recorded by a Tecnai G2 F20 S-TWIN high-resolution transmission electron microscope with an accelerating voltage of 200 kV. High resolution transmission electron microscopy (HRTEM) images were obtained by a JSM-2100 transmission electron microscope (JEOL, Japan). X-ray photoelectron spectra (XPS) were acquired using a Kratos XSAM

800 spectrometer with an Al-K$_\alpha$ X-ray source (h$_v$=1486.6 eV). Inductively coupled plasma atomic emission spectrometer (ICP-AES) was measured on an Agilent 725-ES instrument.

2.4. DFT calculations

The DFT calculations were performed with the Vienna ab initio simulation package (VASP) [30-33], with generalized gradient approximation of Perdew-Burke-Ernzerhof (GGA-PBE) functional as the exchange-correlation functional [34]. The valence electron-core interaction was described by projected augmented wave (PAW) method [35], where the Kohn-Sham equation in the self-consistent calculations have been solved using a cut off energy of 450 eV for the plane wave expansion [36]. 3×3×1 Monkhorst-Pack k-point mesh was used for Brillouin-zone integration. All the structures were relaxed until the residual forces of each atom were less than 0.05 eV/Å and the total energy differences less than $<10^{-7}$ eV. We used p(3×3) supercells with the bottom two layers fixed, while the top two layers fully relaxed for the bulk optimization. The adsorption energy (E_{ads}) of species (A) on metal surface (M) was computed as the difference between the energy of the adsorbed molecule ($E_{tot}^{A/M}$) and the sum of the free surface (E_{tot}^{M}) and the corresponding gas-phase species (E_{tot}^{A}) energies as $E_{ads}=E_{tot}^{A/M}-E_{tot}^{M}-E_{tot}^{A}$.

3. Results and discussion

3.1. Remarkably different kinetics behaviors

The strategy for the decoration of CNT with polymers and subsequent immobilization of Pt catalysts is schematically shown in Fig. 1a. Specifically, the pristine CNT was noncovalently functionalized with the polymers, and the resultant decorated CNT was employed as the catalyst support for the preparation of Pt catalysts via impregnation of H_2PtCl_6 precursor followed by in-situ reduction with AB. As depicted in Fig. 1b, the polymers-decorated CNT supported Pt catalysts show three reaction stages based on the hydrogen generation profiles, where the unsupported pristine and functionalized CNT are completely inactive for this reaction in Fig. S1. According to previous studies [37,38], these could be resultant from as the in-situ reduction of catalyst precursors from Pt^{n+} to Pt^0 with AB and the concomitant ammonia borane hydrolysis to generate hydrogen, followed by the suppressed hydrogen generation at the late reaction stage mainly due to the adsorption of B-containing byproducts. Therefore, it is very crucial to select appropriate reaction stage for elucidating the catalyst structure-performance relations. Herein, considering that the reaction stage under ammonia borane conversions of 20%-50% almost follows zero-order kinetics, it indicates the complete reduction of catalyst precursors and negligible catalytic effects of the deposited B-containing species, which was chosen for the following analysis and discussion.
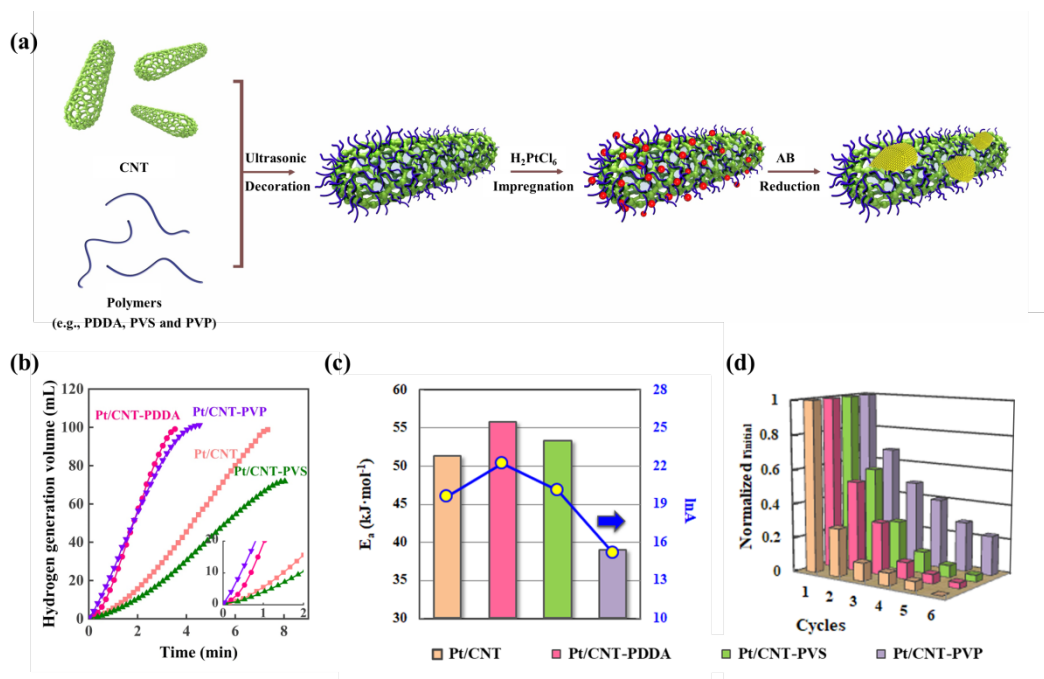
Fig. 1. (a) Schematic diagram for the decoration of CNT with polymers and subsequent immobilization of Pt nanoparticles. (b) The hydrogen generation volume as a function of time at 30 $^{\circ}$C, (c) the activation energy (E_a) and the logarithm of pre-exponential factor (lnA), and (d) the relative activities as a function of catalytic cycle over Pt/CNT, Pt/CNT-PDDA, Pt/CNT-PVS and Pt/CNT-PVP catalysts.

Under ammonia borane conversions of 20%-50%, the reaction rates (r) of the Pt/CNT, Pt/CNT-PDDA, Pt/CNT-PVS and Pt/CNT-PVP catalysts were calculated based on the slope of the linear part for each plot, which were determined as 96.9, 224.3, 70.8, 176.9 $mol_{H2} \cdot mol_{Pt}^{-1} \cdot min^{-1}$, respectively. Obviously, with respect to the pristine Pt/CNT catalyst, the positively charged PDDA-functionalized CNT supported Pt catalyst, i.e., Pt/CNT-PDDA, delivers the highest hydrogen generation rate, while the negatively charged PVS-functionalized CNT supported Pt catalyst, i.e., Pt/CNT-PVS, exhibits the lowest hydrogen generation rate. This is most likely due to the significant effects of the

cationic/anionic polymers on the Pt electronic properties and consequences on the catalytic activities, which will be discussed in detail in Section 3.2.

As shown in the inset of Fig. 1b, the PVP-functionalized CNT supported Pt catalyst, i.e., Pt/CNT-PVP, shows the shortest induction period among all the catalysts. As illustrated in Fig. 1a, during the induction period, the Pt clusters were first generated by the reduction of H_2PtCl_6 precursor with AB, which has been suggested to follow the nucleation and autocatalytic growth mechanism [37]. Typically, the process consists of (a) slow and continuous nucleation, A→B, followed by (b) fast autocatalytic surface growth, A+B→2B, where A and B represent the Pt precursor and resultant Pt surface atoms, respectively. This indicates that the shortest induction period of the Pt/CNT-PVP catalyst is mainly controlled by the fastest Pt nucleation over the PVP-functionalized CNT surface from the standpoint of kinetics. Further combining the capping agent roles of PVP in the shape-controlled growth of metal particles, it is reasonable to deduce the PVP-induced formation of unique geometric Pt nanoparticles for the higher catalytic activity compared with the pristine Pt/CNT catalyst.

To gain insights into the effects of the polymers decoration on the catalytic activity, kinetics experiments of the four catalysts at 25-40 °C were conducted, and the results are shown in Fig. S2. Obviously, under the measured temperature ranges, these catalysts still retain linear relations between the hydrogen generation volume and reaction time under ammonia borane conversions of 20%-50%, implying zero-order kinetics for this reaction. Notably, the observed zero-order kinetics suggest that the reaction is not limited by the external diffusion of reactants. Similarly, the reaction rate (r) and the

corresponding reaction rate constant (k) of each temperature were calculated, and then the Arrhenius plot of lnk versus 1/T yields the activation energy (E_a) as shown in Fig. 1c. Unexpectedly, among these four catalysts, the Pt/CNT-PDDA catalyst with the highest catalytic activity also exhibits the highest activation energy, which indicates another important factor responsible for its highest hydrogen generation rate.

Considering that both the activation energy (E_a) and pre-exponential factor (A) contribute to the reaction rate constant based on the Arrhenius equation, the logarithm of pre-exponential factors (lnA) of these catalysts were further compared in Fig. 1c. Obviously, the highest lnA contributes to the highest hydrogen generation activity of the Pt/CNT-PDDA catalyst. According to the transition state theory, the pre-exponential factor is highly relevant to the enthalpy of activation (ΔS^{0*}), which quantifies the loss of translational freedom upon reactants adsorption [39]. Hence, the Pt/CNT-PDDA catalyst could have the strongest interaction with the reactants in terms of its optimal electronic properties, resulting in the largest loss of translational freedom upon the reactants adsorption. This is consistent with our previous study that the Pt locates at the right side of the volcanic curve, and the large ΔS^{0*} would facilitate hydrogen generation [28].

Moreover, the Pt/CNT-PVP catalyst displays much lower E_a (38.9 kJ·mol^{-1}) compared with the other three catalysts (49.7-55.8 kJ·mol^{-1}). The observed shortest induction period as well as the lowest E_a of the Pt/CNT-PVP catalyst indicates its structural properties far different from the other three catalysts. In our previous study, the Pt(111) has been suggested as the main active sites for this reaction, and its

corresponding activation energy varies from 38 to 41 kJ·mol^{-1} [25], which is similar to that of the Pt/CNT-PVP catalyst. All of these results indicate that the Pt/CNT-PVP catalyst possibly shows preferential exposure of Pt(111) active sites for this reaction.

3.2 Geometric and electronic synergy

The noncovalent functionalization of CNT with the polymers was first studied by Raman spectroscopy, and the results are shown in Fig. 2a. Obviously, two distinct peaks, i.e., D1 and G bands, are displayed for all the supports. Generally, the intensity ratio of D1 band to G band (I_{D1}/I_G) is widely used to quantify the surface defects [40], which is determined to be 1.44, 1.38, 1.41 and 1.51 for the pristine CNT, CNT-PDDA, CNT-PVS and CNT-PVP, respectively. The slightly decreased I_{D1}/I_G ratios for the CNT-PDDA and CNT-PVS most likely arise from the interaction of the defect sites with the PDDA and PVS because of their cationic/anionic natures, while the increased I_{D1}/I_G ratio for the CNT-PVP is possibly due to the creation of new defects by the neutral PVP functionalization. The functionalization of polymers on the CNT surfaces is also evidenced by the blue/red shifts of the G bands when using the positively/negatively charged PDDA/PVS to decorate CNT, as a result of the electron transfer between CNT and polymers [41]. Further FT-IR spectra in Fig. 2b show, apart from the hydroxyl group (3436 cm^{-1}), adsorbed water (1630 cm^{-1}) and C-O bond (1050 cm^{-1}), the stronger bands of -CH$_2$ (2860 cm^{-1}) and -CH$_3$ (2930 cm^{-1}) as a evidence of polymers functionalization [42,43]. Notably, the TGA results in Fig. 2c indicate obvious weight losses over the polymers-functionalized CNT supports compared with the pristine CNT.

In light of such thermal instability, the in-situ reduction with AB rather than the thermal

reduction with H_2 was chosen for the preparation of these polymers-functionalized CNT

supported Pt catalysts.
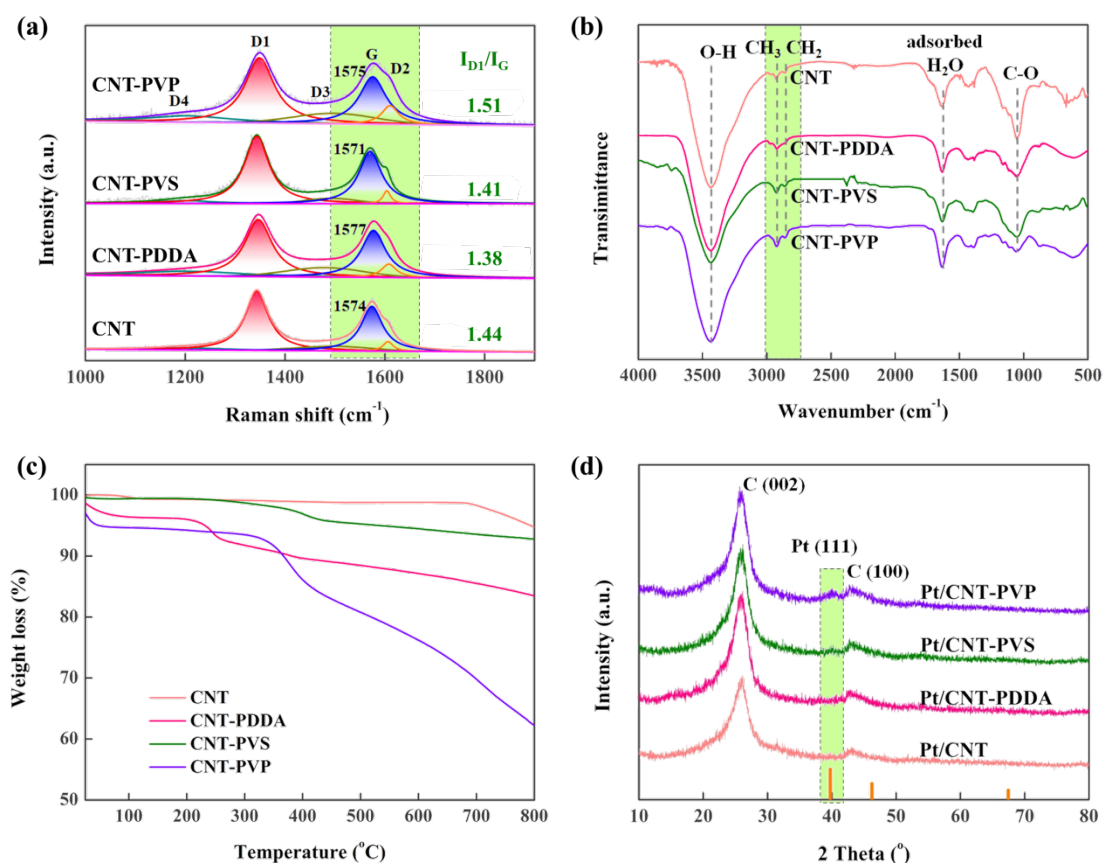
Fig. 2. (a) Raman spectra, (b) FT-IR spectra, and (c) TG profiles of CNT, CNT-PDDA, CNT-PVS

and CNT-PVP. (d) XRD patterns of the reduced Pt/CNT, Pt/CNT-PDDA, Pt/CNT-PVS and Pt/CNT-

PVP catalysts.

Subsequently, the pristine and functionalized CNT supported Pt catalysts were

characterized by XRD. It can be clearly seen in Fig. 2d that there exist only carbon

characteristic diffraction peaks while no legible Pt diffraction peaks for these catalysts

except the Pt/CNT-PVP catalyst, which exhibits a weak peak at 39.8° assigned to

Pt(111). This indicates the large-sized Pt nanoparticles over the CNT-PVP support while the high dispersion of Pt nanoparticles over the other three supports. HAADF-STEM with high resolution was further employed to characterize these four catalysts for obtaining reliable particle size distributions [44]. As shown in Fig. 3, the relatively homogeneous distributions of Pt nanoparticle are observed for the pristine CNT, CNT-PDDA and CNT-PVP supports, while the larger loose Pt aggregates for the CNT-PVP support, consistent with the XRD observations. Furthermore, the average Pt particle sizes of the Pt/CNT, Pt/CNT-PDDA and Pt/CNT-PVS catalysts are respectively determined to be 2.5±0.5, 2.4±0.6 and 2.3±0.7 nm based on the measurements of more than 200 random particles. Considering these three similar-sized Pt catalysts, the size effects could be excluded as the main reason for their remarkably different catalytic activities. Additionally, considering the fast nucleation and growth of Pt particles over the CNT-PVP support as described above, the formed Pt floccules with a rather loose and open structure possibly expose unique surfaces for the enhanced catalytic activity compared with the small-sized Pt/CNT catalyst.
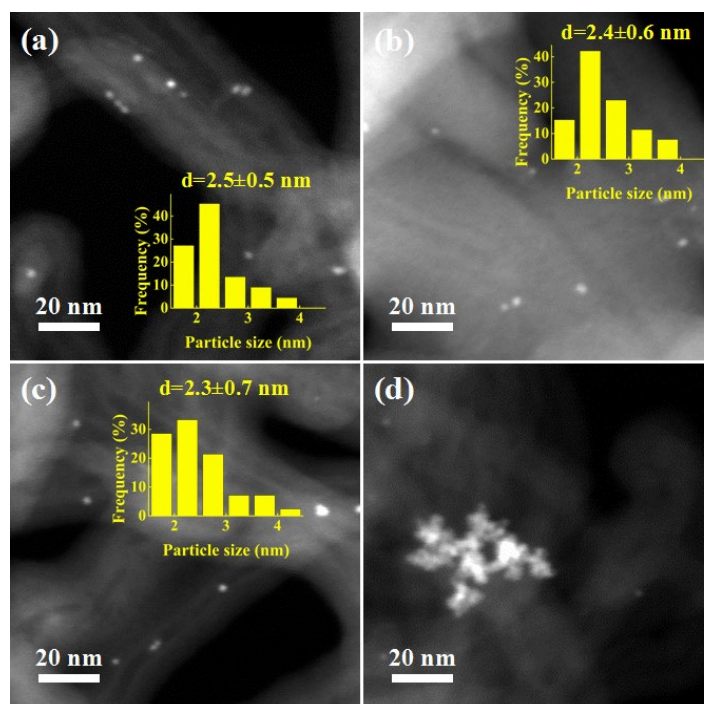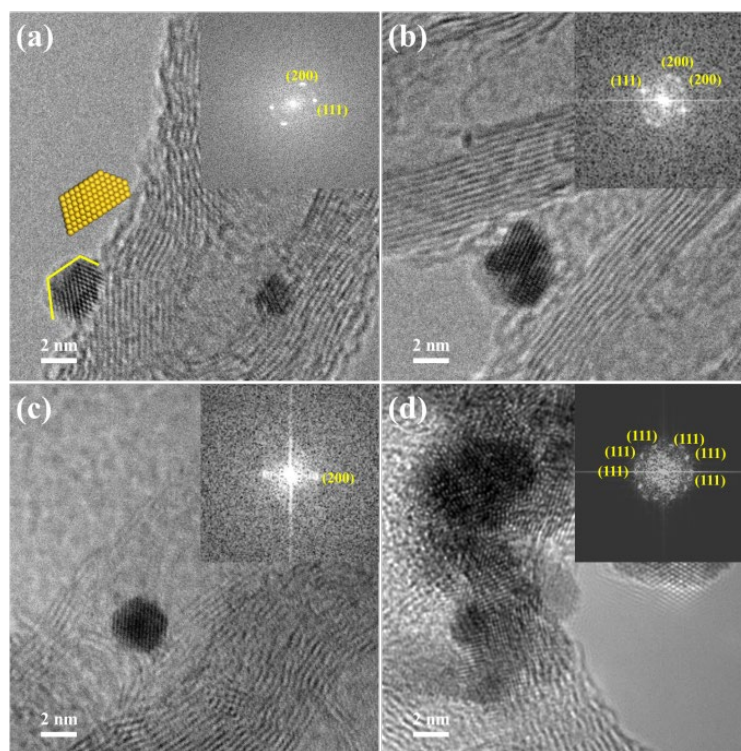
Fig. 3. Typical HAADF-STEM images and the corresponding particle size distributions of the reduced (a) Pt/CNT, (b) Pt/CNT-PDDA, (c) Pt/CNT-PVS and (d) Pt/CNT-PVP catalysts.

HRTEM measurements were further performed to gain more insights into the microstructures of the four Pt catalysts, and the results are shown in Fig. 4. For the small-sized Pt/CNT, Pt/CNT-PDDA and Pt/CNT-PVS catalysts, the fast Fourier transform (FFT) analyses confirm the presence of Pt(111) and Pt(100) crystallographic facets. On the contrary, for the loose aggregated Pt/CNT-PVP catalyst as shown in Fig. 4d, it exhibits a preferential exposure of Pt(111) facet, which could be due to the preferential binding halide to Pt(100) and inhibited growth of Pt(100) by PVP [45,46]. Moreover, a careful statistical analysis as shown in Fig. S3 suggests that the Pt(111) facet accounts for more than 80% of the total exposed facets. Such preferential exposure of the Pt(111) active facet over the Pt/CNT-PVP catalyst could provide a rational

interpretation for the above kinetics analysis, e.g., the lowest E_a of 38.9 kJ·mol^{-1}, which is close to those of our previously reported Pt/CNT catalysts with the Pt(111) as the dominant active sites for the ammonia borane hydrolysis [25]. Additionally, based on the results in Fig. 1c and Fig. 3, although the Pt/CNT-PVP catalyst shows the larger Pt particle size, the preferentially exposed Pt(111) active facets could endow such catalyst with the increased quantity of active sites (N_i) for the relatively high catalytic activity.

Fig. 4. Representative HRTEM images and their corresponding FFT patterns of the reduced (a) Pt/CNT, (b) Pt/CNT-PDDA, (c) Pt/CNT-PVS and (d) Pt/CNT-PVP catalysts.

In addition to the contribution of the quantity of active sites (N_i), that of the electronic properties of the four catalysts is another important issue for the reaction. The XPS spectra in Fig. 5 show that the Pt mainly exists in the form of metallic Pt species for all

the reduced catalysts, and the corresponding binding energy follows the order of Pt/CNT-PDDA (71.90 eV) > Pt/CNT (71.62 eV) > Pt/CNT-PVS (71.60 eV) > Pt/CNT-PVP (71.52 eV). Obviously, the Pt/CNT-PDDA catalyst shows a positive shift (0.28 eV) in the Pt binding energy (B.E.) with respect to the Pt/CNT catalyst, compared with negative shifts for the Pt/CNT-PVS (-0.02 eV) and Pt/CNT-PVP (-0.10 eV) catalysts. Considering the similar Pt particle sizes of the Pt/CNT, Pt/CNT-PDDA and Pt/CNT-PVS catalysts, the trend of the corresponding Pt binding energies suggests that the PDDA acts as the electron-acceptor and captures electrons from the Pt particles, while the PVS acts as the electron-donor and transfers electrons to the Pt particles. Further combining with our previous study [26], the electron-deficient Pt particles with the high binding energy over the CNT-PDDA support facilitate the adsorption of ammonia borane, and cause a large freedom loss upon reactants adsorption as shown in Fig. 1c. Based on the volcanic curve between the ΔS^{0*} and catalytic activity [28], it contributes to the higher quality of active sites (TOF_i). Moreover, for the large-sized Pt/CNT-PVP catalyst with the lowest Pt B.E., its relatively high catalytic activity compared with the Pt/CNT catalyst mainly arises from the preferential exposure of Pt(111) active sites. Therefore, the co-functionalization of CNT with the PDDA and PVP would be expected to improve the quality (TOF_i) and quantity (N_i) of active sites for increasing the reaction rate (r) based on $r=\sum TOF_i \times N_i$, stemming from the electronic and geometric effects, respectively.
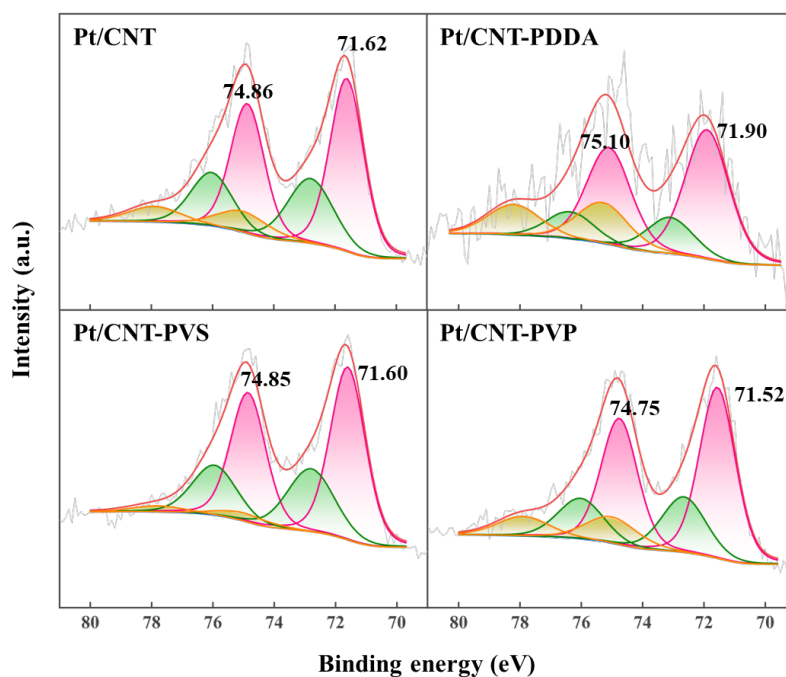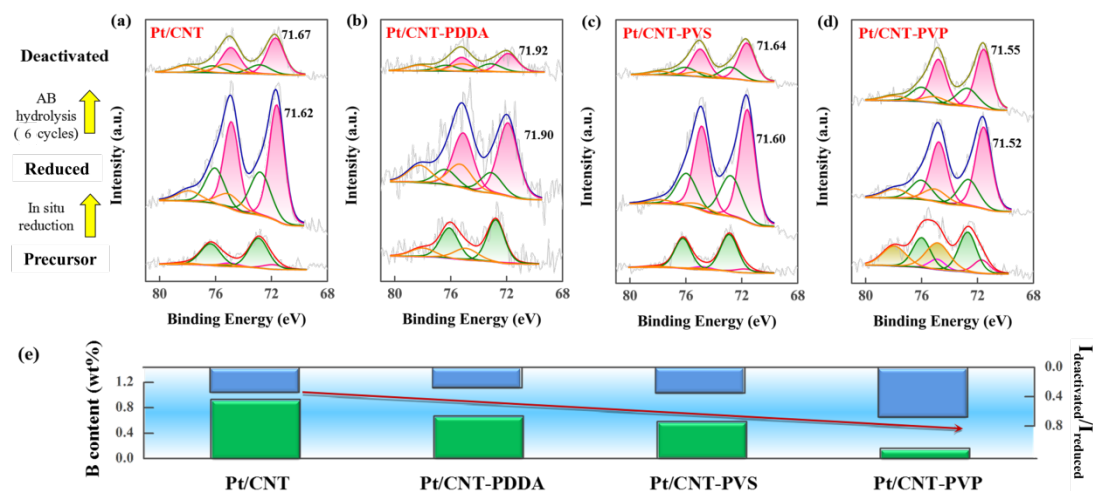
Fig. 5. XPS Pt 4f spectra of the reduced Pt/CNT, Pt/CNT-PDDA, Pt/CNT-PVS and Pt/CNT-PVP catalysts.

3.3 Understanding of catalyst durability

In addition to a stringent requirement for the high catalytic activity, the durability of noble Pt-based catalysts is another important criterion. To this end, the durability of the four catalysts was evaluated by adding another new ammonia borane solution after the completion of the last cycle, and such operation was repeated five times. It can be clearly seen in Fig. S4 that all the catalysts show the decreased activity with the catalytic cycle, and the pristine Pt/CNT catalyst, completely losing catalytic activity at the end of the 5th cycle, suffers from severe deactivation. To make a direct comparison, the reaction rate in each cycle was normalized by that of the first cycle as shown in Fig. 1d. Obviously, the Pt/CNT-PVP catalyst exhibits the highest catalytic durability.

Specifically, at the 6th cycle, the Pt/CNT-PVP catalyst retains 23% of the activity at the first cycle, while the other three catalysts with more severe even complete deactivation. Based on the above TEM observations in Fig. 3, the Pt/CNT-PVP catalyst has shown the largest Pt particle size. Previously, the larger Pt nanoparticles have been also indicated the higher catalyst durability [25]. Therefore, it is rationally deduced that the larger Pt nanoparticles over the Pt/CNT-PVP catalyst is one factor for the highest durability.

To gain more structural insights into the noncovalent functionalization-dependent catalyst durability, HAADF-STEM measurements of the four deactivated catalysts after six cycles were carried out, and the results are shown in Fig. S5. It is observed that a few agglomerations exist over the deactivated Pt/CNT, Pt/CNT-PDDA and Pt/CNT-PVS catalysts. These observations could not explain their remarkably different catalyst durability, in particular, the complete deactivation of the Pt/CNT catalyst after the 5th catalytic cycle. In addition to the agglomeration of Pt nanoparticles, the adsorption of B-containing byproducts on the Pt surfaces has been also suggested as another important factor for the deactivation of Pt catalysts [25], which highly depends on the Pt electronic properties, i.e., the higher Pt binding energy corresponds to the less adsorbed B-containing byproducts and thus the higher catalyst durability [47].

Fig. 6. XPS Pt 4f spectra of the unreduced, reduced and deactivated catalysts of (a) Pt/CNT, (b) Pt/CNT-PDDA, (c) Pt/CNT-PVS and (d) Pt/CNT-PVP. (e) B content and XPS Pt 4f intensity ratio of the deactivated to the reduced catalyst ($I_{deactivated}/I_{reduced}$) for these catalysts.

Along this line, the electronic properties of the four deactivated catalysts were further characterized by XPS. As shown in Fig. 6a-6d, all the deactivated catalysts show upshifts in the Pt 4f B.E., which in principle give rise to the increased catalytic activities according to our previous study on the electronic effects [26, 47]. However, it is opposite to the trend of the observed decreased activities for these catalysts. Meanwhile, the intensity of Pt 4f peak is also observed to become much weaker for the deactivated catalysts, due to the accumulation of by-products (mainly $B(OH)_4^-$ species) over the Pt active sites [47]. In principle, the higher coverage of adsorbates, the more significant decrease of Pt 4f peak intensity. Thus, it is reasonable to compare the Pt 4f peak intensity of the deactivated catalyst with that of the reduced catalyst to evaluate the coverage of reaction by-products. As shown in Fig. 6e, the Pt/CNT-PVP catalyst displays slightly decreased Pt 4f peak intensity compared with the other three catalysts,

following the trend of the catalyst durability. Moreover, the ICP results in Fig. 6e show that the Pt/CNT-PVP catalyst has the lowest content of B-containing species. Hence, a combination of XPS and ICP analyses strongly suggests that the lowest coverage of B-containing byproducts on Pt surfaces contributes to the highest catalytic durability of Pt/CNT-PVP among all the catalysts.

It is noted that according to our previous study [47], the lowest Pt binding energy of Pt/CNT-PVP should favor the adsorption of B-containing species, which is inconsistent with its lowest coverage of B-containing byproducts mentioned above. In other words, this indicates that the durable Pt/CNT-PVP catalyst most likely arises from its unique geometric structure with the preferential exposure of Pt(111) active facet. To support this deduction, we resort to DFT calculations for understanding the effects of Pt crystal facet on the catalyst durability. The Bader charge analysis for the adsorption of $B(OH)_4^-$ on the two primarily exposed facets, i.e., Pt(111) and Pt(100), in Fig. 7a shows the electron transfer from the Pt atoms to the B-containing species, leading to the electron-deficient Pt surfaces. This is in good agreement with the above XPS analysis in Fig. 6a-6d, i.e., the deactivated catalysts with the adsorbed B-containing species exhibiting the increased Pt binding energy. Moreover, as shown in Fig. 7b, the adsorption energy of $B(OH)_4^-$ on the Pt(111) and Pt(100) facet is calculated as -2.29 and -2.58 eV, respectively, suggesting the weak adsorption of the B-containing species on the Pt(111). Therefore, it is reasonable to deduce that the preferentially exposed Pt(111) active facet also inhibits the adsorption of B-containing species, and thus accounts for the highest durability of the Pt/CNT-PVP catalyst.
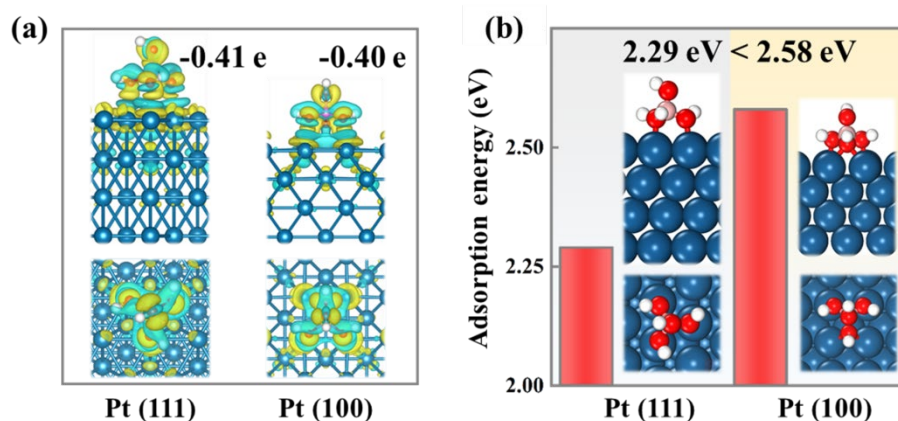
Fig. 7. (a) Isosurfaces of the differential electron density and (b) the absolute adsorption energy for B(OH)$_4^-$ adsorbed on Pt(111) and Pt(100). The yellow and light blue isosurfaces correspond to the electron increase and depletion zone, respectively.

3.4 Mechanism-driven polymer functionalization

To this point, the non-covalent functionalization of CNT with the polymers has significantly affected the geometric and electronic properties of the supported Pt nanoparticles. The Pt(111) facet has emerged as robust sites for hydrogen generation, which not only acts as the dominant active sites for ammonia borane hydrolysis, but also resists the adsorption of B-containing species for enhancing the catalyst durability. Additionally, our previous study has demonstrated that the higher Pt binding energy corresponds to the simultaneously enhanced hydrogen generation activity and catalyst durability [47]. Further combining the electronic effects by PDDA functionalization and the geometric effects by PVP functionalization, it is deduced that co-functionalization of PDDA and PVP might yield an electronic and geometric synergy

to obtain highly active and durable Pt catalyst for this reaction.

To test this idea, the PDDA and PVP were mixed to co-functionalize CNT followed by impregnation with the same amount of Pt. Based on the above analyses, the FT-IR, TGA, Raman and XRD measurements of the as-prepared CNT-PDDA-PVP in Fig. S6 indicate the successful co-functionalization of PDDA and PVP as well as the existence of Pt(111) diffraction peak for the Pt/CNT-PDDA-PVP catalyst. Additionally, the HAADF-STEM and elemental mapping results in Fig. S7 show that the patches of Pt and N from PDDA and PVP exhibit similar shapes, evidencing the interaction of Pt nanoparticles with polymers. Furthermore, the geometric and electronic properties of the Pt/CNT-PDDA-PVP catalyst were characterized by HAADF-STEM, HRTEM and XPS, and the results are shown in Fig. 8. Clearly, the Pt aggregations are still in the form of floccules with a preferential exposure of Pt(111) facet. Similarly, a statistical analysis in Fig. S8 suggests that the Pt(111) facet makes up a high percentage (82%) of the total exposed facets. Moreover, the Pt/CNT-PDDA-PVP catalyst shows a positive shift in the Pt binding energy compared with the Pt/CNT-PVP catalyst. Therefore, the co-functionalization of CNT with PDDA and PVP can combine their merits for the targeted structural properties of Pt nanoparticles, i.e., the preferential exposure of Pt(111) active facet with high Pt binding energy.
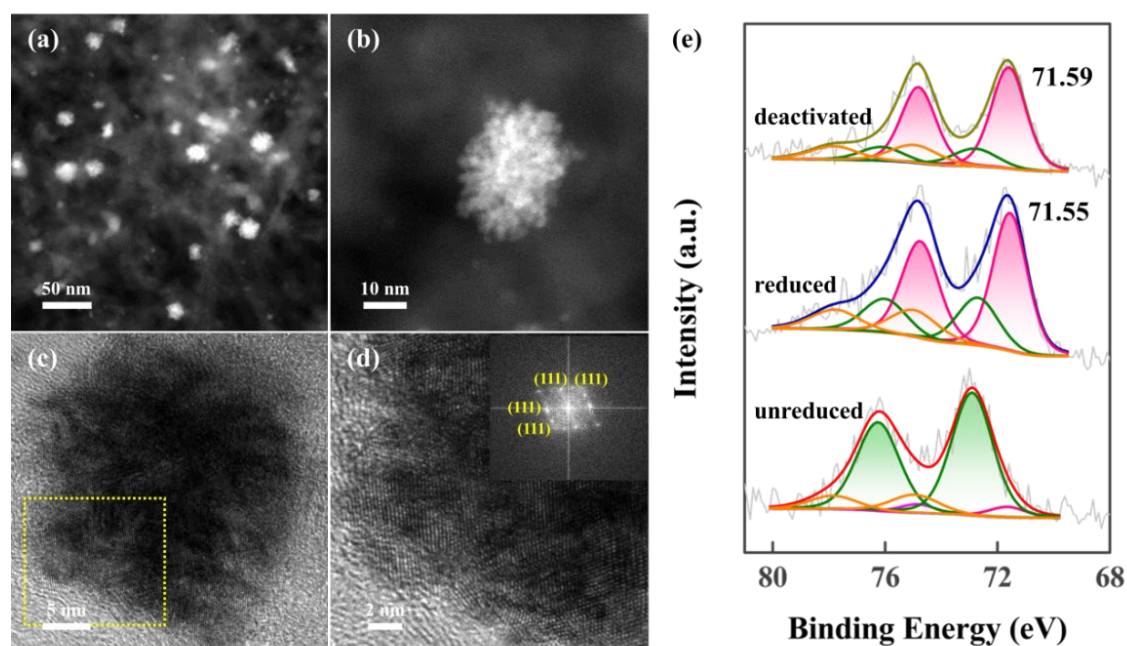
Fig. 8. The (a) low and (b) high magnification HAADF-STEM image of Pt/CNT-PDDA-PVP. The (c) low and (d) high magnification HRTEM image of Pt/CNT-PDDA-PVP. (e) XPS Pt 4f spectra of the unreduced, reduced and deactivated Pt/CNT-PDDA-PVP catalyst.

Kinetics analysis was further conducted to probe the merits of the unique Pt geometric and electronic properties over the Pt/CNT-PDDA-PVP catalyst, and the results are shown in Fig. 9a and 9b. Obviously, this catalyst exhibits medium E_a and lnA values with respect to the Pt/CNT-PDDA and Pt/CNT-PVP catalysts. More interestingly, as shown in Fig. 9c, such trade-off between the E_a and lnA gives rise to the significantly increased hydrogen generation rate. In particular, the PDDA and PVP co-functionalized CNT supported Pt catalyst (290.0 $mol_{H2} \cdot mol_{Pt}^{-1} \cdot min^{-1}$) shows almost three folds higher hydrogen generation rate than the pristine CNT supported Pt catalyst (96.9 $mol_{H2} \cdot mol_{Pt}^{-1} \cdot min^{-1}$). Moreover, as shown in Fig. S9 and 9d, the Pt/CNT-PDDA-

PVP catalyst also exhibits the remarkably enhanced catalyst durability with retaining ca. 34% catalytic activity at the 6th cycle, in which there is still plenty of room to further enhance the durability. In our recent study, the introduction of metal oxides, such as WO_3, onto the CNT support as the sacrificial site has been shown as a more effective strategy to divert the B-containing by-products away from the Pt sites against the deactivation. These results highlight the crucial role of the carbon support decoration and thus the significantly promotional effects of the supported Pt nanoparticles on the hydrogen generation activity and catalyst durability.
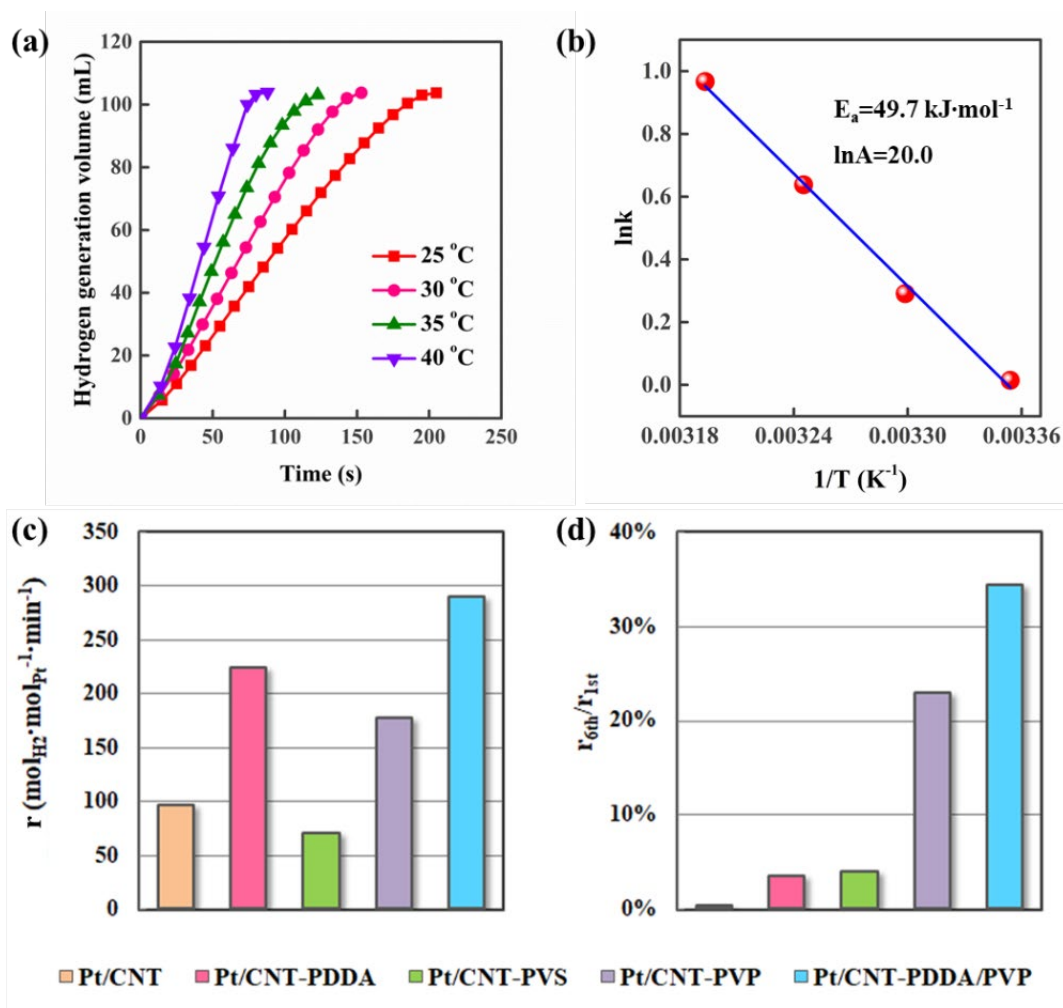
Fig. 9. (a) Hydrogen generation volume as a function of time at 25, 30, 35 and 40 °C, and (b) the corresponding lnk as a function of 1/T for Pt/CNT-PDDA-PVP. (c) The

reaction rate (r) and (d) r_{6th}/r_{1st} for Pt/CNT, Pt/CNT-PDDA, Pt/CNT-PVS, Pt/CNT-PVP and Pt/CNT-PDDA-PVP.

Based on the above results and discussion, the PDDA has been demonstrated as the electron-acceptor to capture electrons from the Pt particles for improved catalytic activity and catalyst durability, while the PVP as the structure-directing agent to induce the preferential exposure of the highly active and durable Pt(111) facet. Combining their merits by co-functionalization has been shown as an effective strategy to achieve a geometric and electronic synergy and thus fabricate highly active and durable Pt-based catalyst for the ammonia borane hydrolysis. Notably, the present study does not involve the optimization of the PDDA/PVP ratio to make full use of their merits and further enhance the activity, durability, or both. This would be facilitated by a combination of theoretical studies with multiple advanced characterization techniques, such as AC-HAADF/STEM, XAS, in-situ XPS and SSITKA, to investigate how the polymers tailor the Pt surface structure, coordination environment and electronic property, and their consequences on the catalytic activity and durability. Therefore, fundamentally understanding these interesting subjects is of crucial importance to guide the rational design of functionalized carbon supported Pt catalysts, which is still ongoing in our group.

4. Conclusions

In summary, we have developed a facile co-functionalization strategy of carbon nanotubes support with the electron-acceptor PDDA and structure-directing-agent PVP, i.e., CNT-PDDA-PVP, to fabricate highly active and durable Pt catalyst for hydrogen generation from ammonia borane. Specifically, the tailored Pt electronic structure by PDDA has contributed to the improved quality of active sites (TOF_i), while the preferential exposure of Pt(111) active facet by PVP to the increased quantity of active sites (N_i). Such electronic and geometric synergy give rise to a 3-fold increase in the catalytic activity as a result of $r=\sum TOF_i \times N_i$. Moreover, a combination of the electron-deficient Pt surfaces with the preferentially exposed Pt(111) within the Pt/CNT-PDDA-PVP catalyst has also significantly promoted the catalyst durability. The encouraging results demonstrated here offer a promising methodology to integrate multiple functionalities with the catalytic centers adapted to the requirements of reaction, which could be extended to the design of other carbon supported catalysts.

Key Laboratory of Chemical Engineering (SKLChe-15C03).

References

[1] P. Serp, M. Corrias, P. Kalck, Carbon nanotubes and nanofibers in catalysis, Appl. Catal. A: Gen. 253 (2003) 337-358.

[2] J. Zhu, A. Holmen, D. Chen, Carbon nanomaterials in catalysis: proton affinity, chemical and electronic properties, and their catalytic consequences, ChemCatChem 5 (2013) 378-401.

[3] D.S. Su, R. Schlogl, Nanostructured carbon and carbon nanocomposites for electrochemical energy storage applications, ChemSusChem 3 (2010) 136-168.

[4] Y.B. Yan, J.W. Miao, Z.H. Yang, F.X. Xiao, H.B. Yang, B. Liu, Y.H. Yang, Carbon nanotube catalysts: recent advances in synthesis, characterization and applications, Chem. Soc. Rev. 44 (2015) 3295-3346.

[5] S.Y. Wang, D.S. Yu, L.M. Dai, Polyelectrolyte functionalized carbon nanotubes as efficient metal-free electrocatalysts for oxygen reduction, J. Am. Chem. Soc. 133 (2011) 5182-5185.

[6] J.D. Roy-Mayhew, D.J. Bozym, C. Punckt, I.A. Aksay, Functionalized graphene as a catalytic counter electrode in dye-sensitized solar cells, ACS Nano 4 (2010) 6203-6211.

[7] X.M. Gu, W. Qi, S.C. Wu, Z.H. Sun, X.Z. Xu, D.S. Su, Noncovalent functionalization of multi-walled carbon nanotubes as metal-free catalysts for the reduction of nitrobenzene, Catal. Sci. Tech. 4 (2014) 1730-1733.

[8] J. Chen, H. Liu, W. A. Weimer, M.D. Halls, D.H. Waldeck, G.C. Walker, Noncovalent engineering of carbon nanotube surfaces by rigid, functional conjugated polymers, J. Am. Chem. Soc. 124 (2002) 9034-9035.

[9] V. Georgakilas, M. Otyepka, A.B. Bourlinos, V. Chandra, N. Kim, K.C. Kemp, P. Hobza, R. Zboril, K.S. Kin, Functionalization of graphene: covalent and non-covalent approaches, derivatives and applications, Chem. Rev. 112 (2012) 6156-6214.

[10] D. Tuncel, Non-covalent interactions between carbon nanotubes and conjugated polymers, Nanoscale 3 (2011) 3545-3554.

[11] H. Wu, W. Zhao, H. Hu, G. Chen, One-step in situ ball milling synthesis of polymer-functionalized graphene nanocomposites, J. Mater. Chem. 21 (2011) 8626-8632.

[12] R.K. Layek, A.K. Nandi, A review on synthesis and properties of polymer functionalized graphene, Polymer 54 (2013) 5087-5103.

[13] S.Y. Wang, S.P. Jiang, X. Wang, Polyelectrolyte functionalized carbon nanotubes as a support for noble metal electrocatalysts and their activity for methanol oxidation, Nanotechnology 19 (2008) 265601.

[14] S.Y. Wang, X. Wang, S.P. Jiang, PtRu nanoparticles supported on 1-aminopyrene-functionalized multiwalled carbon nanotubes and their electrocatalytic activity for methanol oxidation, Langmuir 24 (2008) 10505-10512.

[15] S.Y. Wang, D.S. Yu, L.M. Dai, D.W. Chang, J.B. Baek, Polyelectrolyte-functionalized graphene as metal-free electrocatalysts for oxygen reduction, ACS Nano 5 (2011) 6202-6209.

[16] X. Wang, D.P. Liu, S.Y. Song, H.J. Zhang, Synthesis of highly active Pt-CeO$_2$ hybrids with tunable secondary nanostructures for the catalytic hydrolysis of ammonia borane, Chem. Commun. 82 (2012) 10207-10209.

[17] M.A. Khalily, H. Eren, S. Akbayrak, H.H. Susapto, N. Biyikli, S. Ozkar, M.O. Guler, Facile synthesis of three-dimensional Pt-TiO$_2$ nano-networks: A highly active catalyst for the hydrolytic dehydrogenation of ammonia-borane, Angew. Chem. Int. Ed. 55 (2016) 12257-12261.

[18] S. Wang, D. Zhang, Y.Y. Ma, H. Zhang, J. Gao, Y.T. Nie, X.H. Sun, Aqueous solution synthesis of Pt-M (M= Fe, Co, Ni) bimetallic nanoparticles and their catalysis for the hydrolytic dehydrogenation of ammonia borane, ACS Appl. Mater. Int. 6 (2014) 12429-12435.

[19] Z. Li, T. He, D. Matsumura, S. Miao, A.A. Wu, L. Liu, G.T. Wu, P. Chen, Atomically dispersed Pt on the surface of Ni particles: synthesis and catalytic function in hydrogen generation from aqueous ammonia-borane, ACS Catal. 7 (2017) 6762-6769.

[20] J.K. Zhang, C.Q. Chen, S. Chen, Q.M. Hu, Z. Gao, Y.Q. Li, Y. Qin, Highly dispersed Pt nanoparticles supported on carbon nanotubes produced by atomic layer deposition for hydrogen generation from hydrolysis of ammonia borane, Catal. Sci. Tech. 7 (2017) 322-329.

[21] H.L. Jiang, Q. Xu, Catalytic hydrolysis of ammonia borane for chemical hydrogen storage, Catal. Today 170 (2011) 56-63.

[22] J.M. Yan, X.B. Zhang, H. Shioyama, Q. Xu, Room temperature hydrolytic dehydrogenation of ammonia borane catalyzed by Co nanoparticles, J. Power Sources 195 (2010) 1091-1094.

[23] O. Metin, S. Ozkar, S.H. Sun, Monodisperse nickel nanoparticles supported on SiO_2 as an effective catalyst for the hydrolysis of ammonia-borane, Nano Res. 3 (2010) 676-684.

[24] W.W. Zhan, Q.L. Zhu, Q. Xu, Dehydrogenation of ammonia borane by metal nanoparticle catalysts, ACS Catal. 6 (2016) 6892-6905.

[25] W.Y. Chen, J. Ji, X. Feng, X.Z. Duan, G. Qian, P. Li, X.G. Zhou, D. Chen, W.K. Yuan, Mechanistic insight into size-dependent activity and durability in Pt/CNT catalyzed hydrolytic dehydrogenation of ammonia borane, J. Am. Chem. Soc. 136 (2014) 16736-16739.

[26] W.Y. Chen, J. Ji, X.Z. Duan, G. Qian, P. Li, X.G. Zhou, D. Chen, W.K. Yuan, Unique reactivity in Pt/CNT catalyzed hydrolytic dehydrogenation of ammonia borane, Chem. Commun. 50 (2014) 2142-2144.

[27] W.Y. Chen, D.L. Li, Z.J. Wang, G. Qian, Z.J. Sui, X.Z. Duan, X.G. Zhou, I. Yeboah, D. Chen, Reaction mechanism and kinetics for hydrolytic dehydrogenation of ammonia borane on a Pt/CNT catalyst, AIChE J. 63 (2014) 60-65.

[28] W.Y. Chen, D.L. Li, C. Peng, G. Qian, X.Z. Duan, D. Chen, X.G. Zhou, Mechanistic and kinetic insights into the Pt-Ru synergy during hydrogen generation from ammonia borane over PtRu/CNT nanocatalysts, J. Catal. 356 (2017) 186-196.

[29] E. Gottlieb, K. Matyjaszewski, T. Kowalewski, Polymer-based synthetic routes to carbon-based metal-free catalysts, Adv. Mater. 31 (2019) 1804626.

[30] G. Kresse, J. Hafner, Ab inito molecular dynamics for metals, Phys. Rev. B 47 (1993) 558-561.

[31] G. Kresse, J. Hafner, Ab initio molecular-dynamics simulation of the liquid-metal-amorphous-semiconductor transition in germanium, Phys. Rev. B 49 (1994) 14251-14269.

[32] G. Kresse, J. Furthmüller, Efficiency of ab-initio total energy calculations for metals and semiconductors using a plane-wave basis set, Comput. Mater. Sci. 6 (1996) 15-50.

[33] G. Kresse, J. Furthmüller, Efficient iterative schemes for ab-initio total-energy calculations using a plane-wave basis set, Phys. Rev. B 54 (1996) 11169-11186.

[34] J.P. Perdew, K. Burke, M. Ernzerhof, Generalized gradient approximation made simple, Phys. Rev. Lett. 77 (1996) 3865-3868.

[35] P.E. Blöchl, Projector Augmented-Wave Method, Phys. Rev. B 50 (1994) 17953-17979.

[36] H.J. Monkhorst, J.D. Pack, Special points for Brillouin-zone Integrations, Phys. Rev. B 13 (1976) 5188-5192.

[37] S. Akbayrak, S. Ozkar, Ruthenium (0) nanoparticles supported on multiwalled carbon nanotube as highly active catalyst for hydrogen generation from ammonia-borane, ACS Appl. Mater. Inter. 4 (2012) 6302-6310.

[38] H. Erdogan, O. Metin, S. Ozkar, In situ-generated PVP-stabilized palladium (0) nanocluster catalyst in hydrogen generation from the methanolysis of ammonia-borane, Phys. Chem. Chem. Phys. 11 (2009) 10519-10525.

[39] H. Ma, C. Na, Isokinetic temperature and size-controlled activation of ruthenium-catalyzed ammonia borane hydrolysis, ACS Catal. 5 (2015) 1726-1735.

[40] A. Sadezky, H. Muckenhuber, H. Grothe, R. Niessner, U. Poschl, Raman microspectroscopy of soot and related carbonaceous materials: spectral analysis and structural information, Carbon 43 (2005) 1731-1742.

[41] L. Dennany, P. Sherrell, J. Chen, P.C. Innis, G.G. Wallace, A.I. Minett, EPR characterisation of platinum nanoparticle functionalised carbon nanotube hybrid materials, Phys. Chem. Chem. Phys. 12 (2010) 4135-4141.

[42] S.I. Cha, K.T. Kim, K.H. Lee, C.B. Mo, Y.J. Jeong, S.H. Hong, Mechanical and electrical properties of cross-linked carbon nanotubes, Carbon 46 (2008) 482-488.

[43] C. Chang, B. Duan, J. Cai, L. Zhang, Superabsorbent hydrogels based on cellulose for smart swelling and controllable delivery, Eur. Polym. J. 46 (2010) 92-100.

[44] B. Zhang, W. Zhang, D.S. Su, Towards a more accurate particle size distribution of supported catalyst by using HAADF-STEM, ChemCatChem 3 (2011) 965-968.

[45] J. Xu, G. Fu, Y. Tang, Y. Zhou, Y. Chen, T. Lu, One-pot synthesis of three-dimensional platinum nanochain networks as stable and active electrocatalysts for oxygen reduction reactions, J. Mater. Chem. 22 (2012) 13585-13590.

[46] J. Chen, B. J. Wiley, Y. Xia, One-dimensional nanostructures of metals: large-scale synthesis and some potential applications, Langmuir 23 (2007) 4120-4129.

[47] W. Chen, X. Duan, G. Qian, D. Chen, X. Zhou, Carbon nanotubes as support in the platinum-catalyzed hydrolytic dehydrogenation of ammonia borane. ChemSusChem 8 (2015) 2927-2931.